

EFFECT OF TEMPERATURE AND MULTIPLE SCATTERING ON RAIN ATTENUATION OF ELECTROMAGNETIC WAVES BY A SIMPLE SPHERICAL MODEL

E. Setijadi, A. Matsushima, and N. Tanaka

Graduate School of Science and Technology
Kumamoto University
2-39-1 Kurokami, Kumamoto 860-8555, Japan

G. Hendranto

Jurusan Teknik Elektro
Institut Teknologi Sepuluh Nopember
Kampus ITS Sukolilo, Surabaya 60111, Indonesia

Abstract—Specific rain attenuation is discussed from the viewpoint of numerical solution for scattering and absorption of electromagnetic waves related to dielectric spheres. Special attention is paid to the quantitative evaluations considering the change of temperature and the existence of multiple scattering effect. The analysis is based on the set of Stratton’s vector spherical wave functions and its addition theorem, which lead to the simultaneous linear equations for the expansion coefficients with adaptively selected truncation numbers. Computed extinction cross sections lead directly to the specific rain attenuation, where the Weibull raindrop distribution model is used. It is discussed how the dependence of the permittivity of water on temperature and frequency affects the attenuation property. Furthermore, the effect of multiple scattering is evaluated in terms of the root mean square of attenuation deviation from the simple superposition of single scattering (Mie’s) coefficients. Contrary to general belief, this deviation is the highest at around the boundary between microwave and millimeter wave bands.

1. INTRODUCTION

The attenuation by rain medium has received much attention [1–4], since it is closely related to the quality of communication systems.

Corresponding author: A. Matsushima (matsua@cs.kumamoto-u.ac.jp).

Scattering and absorption of electromagnetic waves by small droplets of water cause this attenuation, and the amount of it is usually indicated by the specific rain attenuation in dB/km as a function of frequency and rainfall intensity. A lot of works have been reported concerning the above effect from the viewpoints of

- deterioration of cross polarization discrimination due to the tilt of vertical axis by wind [4, 5]
- change of temperature [4]
- incorporation of multiple scattering [6–8].

The top item concerning cross polarization requires the data of distortion of raindrop shape from a sphere, e.g., by the famous model by Pruppacher et al. [9]. The consideration of the other two items, temperature and multiple scattering, also become precise when taking account of the distortion of drops. It is said that multiple scattering effects are small in the low frequency region but cannot be neglected at high frequencies. Previous investigations stated that this threshold is about 30 GHz [6], and that slight difference occurs between the models of first order and complete multiple scattering at 30 GHz for precipitation more than 100 mm/h [7]. Furthermore, Twersky's scattering formalism clarified that the multiple scattering is negligible up to at least 1 THz for coherent transmission [8]. In spite of all these works dealing with multiple scattering, it is still an important task to quantitatively evaluate the interaction among realistic raindrops distribution in a numerically exact manner. With regard to this, we can make use of an effective tool based on the multipole expansion [10–12], and thereby it is expected that even the spherical model yields quantitative information to some extent. This is why we choose this simple model as a starting point.

On the situations above, we seek for the effect of temperature and multiple scattering on the amount of attenuation from the numerical point of view. Employing the set of Stratton's vector spherical wave functions [13], combined with its addition theorem [14] and orthogonal property [13], we obtain the simultaneous linear equations for the expansion coefficients of electromagnetic fields. This procedure is the same as that of Ref. [11], except that we make an adaptive choice of the truncation numbers according to the sphere size to reduce the CPU time. The specific rain attenuation can be evaluated directly from the extinction cross section of a set of raindrops, which are randomly allocated inside a big fictitious sphere. Among a lot of distribution models to determine the raindrop size, including classical Marshall and Palmer's [15] and the Gamma one [16], we select the Weibull model [17], because it was reported that the last model yields the best

agreement with the experimental data [18]. As for the permittivity of water, we use Liebe’s formula [19] since it works up to 1 THz and covers the low frequency region where Debye type expression is effective.

Numerical results are demonstrated for the rain attenuation as a function of frequency, rainfall intensity, and temperature. We discuss the deviation of root mean square between our approach and the Mie’s solution [20], the latter of which neglects the multiple scattering terms. It will be shown that this deviation has a peak around the boundary between microwave and millimeter wave bands depending on the rainfall.

2. NUMERICAL METHOD

2.1. Field Expressions

Figure 1 shows a set of Q dielectric spheres arbitrarily distributed in the air. The spheres have a common relative permittivity ϵ_r , and each has a radius of a_q ($q = 1, 2, \dots, Q$).

The total electromagnetic fields outside the spheres are decomposed into $(\mathbf{E}^i, \mathbf{H}^i) + \sum_{q=1}^Q (\mathbf{E}^{s(q)}, \mathbf{H}^{s(q)})$, where the superscripts i and $s(q)$ concern the incident field and the scattered field emitted from the q -th sphere, respectively. The field penetrating into the p -th sphere is denoted by $(\mathbf{E}^{d(p)}, \mathbf{H}^{d(p)})$. With no loss of generality, we can assume that the incident field is an x -polarized plane wave with unit electric field amplitude which propagates in the $+z$ direction. Omitting the

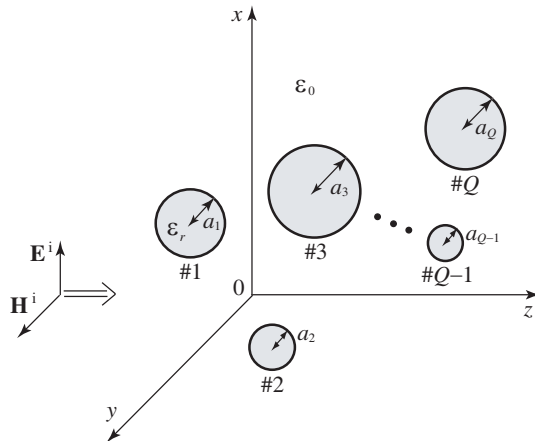


Figure 1. Spherical scatterers and an incident plane wave.

time factor $e^{j\omega t}$, we write the above fields in terms of the multipole coefficients and the vector spherical wave functions [13] as

$$\begin{pmatrix} \mathbf{E}^i(\mathbf{r}) \\ -j\zeta_0 \mathbf{H}^i(\mathbf{r}) \end{pmatrix} = e^{-jk_0 z_{p0}} \sum_{n=1}^{\infty} \sum_{m=-n}^n \begin{pmatrix} V_{mn} & U_{mn} \\ U_{mn} & V_{mn} \end{pmatrix} \begin{pmatrix} \mathbf{M}_{mn}^{(1)}(k_0 \mathbf{r}_p) \\ \mathbf{N}_{mn}^{(1)}(k_0 \mathbf{r}_p) \end{pmatrix} \quad (1)$$

$$\begin{pmatrix} \mathbf{E}^{s(q)}(\mathbf{r}) \\ -j\zeta_0 \mathbf{H}^{s(q)}(\mathbf{r}) \end{pmatrix} = \sum_{n=1}^{\infty} \sum_{m=-n}^n \begin{pmatrix} B_{qmn} & A_{qmn} \\ A_{qmn} & B_{qmn} \end{pmatrix} \begin{pmatrix} \mathbf{M}_{mn}^{(4)}(k_0 \mathbf{r}_q) \\ \mathbf{N}_{mn}^{(4)}(k_0 \mathbf{r}_q) \end{pmatrix} \quad (2)$$

$$\begin{pmatrix} \mathbf{E}^{d(p)}(\mathbf{r}) \\ -j\zeta \mathbf{H}^{d(p)}(\mathbf{r}) \end{pmatrix} = \sum_{n=1}^{\infty} \sum_{m=-n}^n \begin{pmatrix} D_{pmn} & C_{pmn} \\ C_{pmn} & D_{pmn} \end{pmatrix} \begin{pmatrix} \mathbf{M}_{mn}^{(1)}(k \mathbf{r}_p) \\ \mathbf{N}_{mn}^{(1)}(k \mathbf{r}_p) \end{pmatrix} \quad (3)$$

where $k_0 = \omega \sqrt{\epsilon_0 \mu_0}$, $k = k_0 \sqrt{\epsilon_r}$, $\zeta_0 = \sqrt{\mu_0 / \epsilon_0}$, and $\zeta = \zeta_0 / \sqrt{\epsilon_r}$. The symbols \mathbf{r} and \mathbf{r}_p stand for the global and local position vectors, respectively. That is, letting \mathbf{r}_{p0} be a global position of the center of the p -th sphere, we have the relation $\mathbf{r} = \mathbf{r}_{p0} + \mathbf{r}_p$. The arguments $k_0 \mathbf{r}_p$ and $k \mathbf{r}_p$ in Eqs. (1)–(3) mean $(k_0 r_p, \theta_p, \phi_p)$ and $(k r_p, \theta_p, \phi_p)$, respectively.

The vector spherical wave functions in Eq. (2) are defined by

$$\mathbf{M}_{mn}^{(4)}(\rho, \theta, \phi) = h_n^{(2)}(\rho) \mathbf{m}_{mn}(\theta, \phi) \quad (4)$$

$$\begin{aligned} \mathbf{N}_{mn}^{(4)}(\rho, \theta, \phi) &= [jn(n+1)/\rho] h_n^{(2)}(\rho) \sin \theta \pi_n^{|m|}(\theta) e^{jm\phi} \hat{r} \\ &+ \left\{ \left[\rho h_n^{(2)}(\rho) \right]' / \rho \right\} \mathbf{n}_{mn}(\theta, \phi) \end{aligned} \quad (5)$$

where $\mathbf{m}_{mn}(\theta, \phi) = \mathbf{n}_{mn} \times \hat{r} = \left[-m \pi_n^{|m|}(\theta) \hat{\theta} - j \tau_n^{|m|}(\theta) \hat{\phi} \right] e^{jm\phi}$, $\pi_n^m(\theta) = P_n^m(\cos \theta) / \sin \theta$, and $\tau_n^m(\theta) = dP_n^m(\cos \theta) / d\theta$, with $h_n^{(2)}$ and P_n^m being the spherical Hankel function of the second kind and the associated Legendre function, respectively. The definitions of $\mathbf{M}_{mn}^{(1)}$ and $\mathbf{N}_{mn}^{(1)}$ are identical with Eqs. (4) and (5), except that $h_n^{(2)}$ is replaced by the spherical Bessel function j_n .

As for the incident field of Eq. (1), the formula for the spherical wave expansion of a plane wave [13] yields $U_{mn} = -\text{sgn}(m) V_{mn} = -j^{-n} (2n+1) \delta_{|m|1} / [2n(n+1)]$, where $\delta_{|m|1}$ is Kronecker's delta.

2.2. Discretization

The boundary condition on the dielectric surface is written as

$$\begin{aligned} \hat{r}_p \times \left(\mathbf{F}^i(\mathbf{r}) + \sum_{q=1}^Q \mathbf{F}^{s(q)}(\mathbf{r}) - \mathbf{F}^{d(p)}(\mathbf{r}) \right) \Big|_{r_p=a_p} &= 0 \\ (0 \leq \theta_p \leq \pi, 0 \leq \phi_p < 2\pi; p = 1, 2, \dots, Q) & \quad (6) \end{aligned}$$

where \mathbf{F} stands for \mathbf{E} and \mathbf{H} . We substitute Eqs. (1)–(3) into Eq. (6) and truncate the infinite series at $n = N_q$ for the q -th sphere ($q = 1, 2, \dots, Q$) according to its size. This leads us to linear equations including $4 \sum_{q=1}^Q N_q(N_q + 2)$ unknown coefficients A_{qmn} , B_{qmn} , C_{pmn} , and D_{pmn} .

As seen from the right hand sides of Eqs. (1)–(3), the origins of observation points are not unified at the present stage. In order to shift the origin of $(\mathbf{E}^{\mathbf{s}(q)}, \mathbf{H}^{\mathbf{s}(q)})$ from \mathbf{r}_{q0} to \mathbf{r}_{p0} , we apply the addition theorem for vector spherical wave functions [14]

$$\begin{pmatrix} \mathbf{M}_{mn}^{(4)}(k_0 \mathbf{r}_q) \\ \mathbf{N}_{mn}^{(4)}(k_0 \mathbf{r}_q) \end{pmatrix} = \sum_{\nu=1}^{\infty} \sum_{\mu=-\nu}^{\nu} \begin{pmatrix} \alpha_{mn,\mu\nu}^{(4)}(k_0 \mathbf{r}_{pq}) & \beta_{mn,\mu\nu}^{(4)}(k_0 \mathbf{r}_{pq}) \\ \beta_{mn,\mu\nu}^{(4)}(k_0 \mathbf{r}_{pq}) & \alpha_{mn,\mu\nu}^{(4)}(k_0 \mathbf{r}_{pq}) \end{pmatrix} \times \begin{pmatrix} \mathbf{M}_{\mu\nu}^{(1)}(k_0 \mathbf{r}_p) \\ \mathbf{N}_{\mu\nu}^{(1)}(k_0 \mathbf{r}_p) \end{pmatrix} \quad (|\mathbf{r}_p| < |\mathbf{r}_{pq}|) \quad (7)$$

The translation coefficients $\alpha_{mn,\mu\nu}^{(4)}$ and $\beta_{mn,\mu\nu}^{(4)}$ depend on the shift vector $\mathbf{r}_{pq} = \mathbf{r}_{p0} - \mathbf{r}_{q0}$. Making use of the orthogonal properties of the vector spherical wave functions [13], and eliminating the coefficients $C_{p\mu\nu}$ and $D_{p\mu\nu}$, we arrive at the set of linear equations

$$\begin{pmatrix} A_{p\mu\nu} \\ B_{p\mu\nu} \end{pmatrix} - \sum_{\substack{q=1 \\ (q \neq p)}}^Q \sum_{n=1}^{N_q} \sum_{m=-n}^n \begin{pmatrix} \alpha_{mn,\mu\nu}^{(4)} \bar{A}_{p\nu} & \beta_{mn,\mu\nu}^{(4)} \bar{A}_{p\nu} \\ \beta_{mn,\mu\nu}^{(4)} \bar{B}_{p\nu} & \alpha_{mn,\mu\nu}^{(4)} \bar{B}_{p\nu} \end{pmatrix} \begin{pmatrix} A_{qmn} \\ B_{qmn} \end{pmatrix} = \begin{pmatrix} U_{\mu\nu} \bar{A}_{p\nu} \\ V_{\mu\nu} \bar{B}_{p\nu} \end{pmatrix} e^{-jk_0 z_{p0}} \begin{pmatrix} \nu = 1, 2, \dots, N_p; \\ \mu = -\nu, -\nu + 1, \dots, \nu; \\ p = 1, 2, \dots, Q \end{pmatrix} \quad (8)$$

where the argument $k_0 \mathbf{r}_{pq}$ for $\alpha_{mn,\mu\nu}^{(4)}$ and $\beta_{mn,\mu\nu}^{(4)}$ has been omitted for simplicity, and

$$\bar{A}_{p\nu} = -\frac{J_{p\nu} \tilde{J}'_{p\nu} - \sqrt{\varepsilon_r} J'_{p\nu} \tilde{J}_{p\nu}}{\Delta_{p\nu}^{(1)}}, \quad \bar{B}_{p\nu} = -\frac{J'_{p\nu} \tilde{J}_{p\nu} - \sqrt{\varepsilon_r} J_{p\nu} \tilde{J}'_{p\nu}}{\Delta_{p\nu}^{(2)}} \quad (9)$$

with $J_{p\nu} = k_0 a_p j_\nu(k_0 a_p)$, $\tilde{J}_{p\nu} = k a_p j_\nu(k a_p)$, $H_{p\nu} = k_0 a_p h_\nu^{(2)}(k_0 a_p)$, $\Delta_{p\nu}^{(1)} = H_{p\nu} \tilde{J}'_{p\nu} - \sqrt{\varepsilon_r} H'_{p\nu} \tilde{J}_{p\nu}$, and $\Delta_{p\nu}^{(2)} = H'_{p\nu} \tilde{J}_{p\nu} - \sqrt{\varepsilon_r} H_{p\nu} \tilde{J}'_{p\nu}$. The prime in $J'_{p\nu}$, $\tilde{J}'_{p\nu}$, and $H'_{p\nu}$ denotes differentiation with respect to the variable $k_0 r$ or kr . Eq. (8) includes the same number of relations as that of unknowns, and thereby, is numerically solved. After that, the other coefficients are computed from

$$C_{p\mu\nu} = \bar{C}_{p\nu} A_{p\mu\nu} / \bar{A}_{p\nu}, \quad D_{p\mu\nu} = \bar{D}_{p\nu} B_{p\mu\nu} / \bar{B}_{p\nu} \quad (10)$$

where

$$\bar{C}_{p\nu} = j\sqrt{\varepsilon_r}/\Delta_{p\nu}^{(1)}, \quad \bar{D}_{p\nu} = -j\sqrt{\varepsilon_r}/\Delta_{p\nu}^{(2)} \quad (11)$$

Eqs. (9) and (11) represent the set of Mie coefficients [20].

2.3. Conversion to Specific Rain Attenuation

Use of the asymptotic expressions of the spherical Hankel functions in Eqs. (4) and (5) permits us to write the far scattered field $(\mathbf{E}^s, \mathbf{H}^s) = \sum_{q=1}^Q (\mathbf{E}^{s(q)}, \mathbf{H}^{s(q)})$ in the form of inhomogeneous spherical waves as

$$\begin{pmatrix} E_\theta^s(\mathbf{r}) \\ E_\phi^s(\mathbf{r}) \end{pmatrix} \approx \begin{pmatrix} \zeta_0 H_\phi^s(\mathbf{r}) \\ -\zeta_0 H_\theta^s(\mathbf{r}) \end{pmatrix} \approx \frac{e^{-jk_0 r}}{k_0 r} \begin{pmatrix} f_\theta(\theta, \phi) \\ f_\phi(\theta, \phi) \end{pmatrix} \quad (r \rightarrow \infty) \quad (12)$$

where the pattern functions f_θ and f_ϕ are written in terms of A_{qmn} and B_{qmn} . The total scattered power is computed from

$$\begin{aligned} P^s &= \frac{1}{2} \operatorname{Re} \left[\int_0^{2\pi} \int_0^\pi [\mathbf{E}^s(\mathbf{r}) \times \mathbf{H}^{s*}(\mathbf{r})] \cdot \hat{r} \Big|_{r \rightarrow \infty} r^2 \sin \theta \, d\theta \, d\phi \right] \\ &\approx \frac{1}{2\zeta_0 k_0^2} \int_0^{2\pi} \int_0^\pi [|f_\theta(\theta, \phi)|^2 + |f_\phi(\theta, \phi)|^2] \sin \theta \, d\theta \, d\phi \quad (13) \end{aligned}$$

where the asterisk denotes complex conjugate. Since the power density of incident field is $W^i = 1/(2\zeta_0)$, the total scattering cross section is given by $\sigma^s = P^s/W^i = 2\zeta_0 P^s$.

Similarly, the power absorbed inside the spheres is defined by

$$\begin{aligned} P^a &= \frac{1}{2} \operatorname{Re} \sum_{q=1}^Q \left[\int_0^{2\pi} \int_0^\pi [\mathbf{E}^{d(q)}(\mathbf{r}) \times \mathbf{H}^{d(q)*}(\mathbf{r})] \cdot (-\hat{r}_q) \Big|_{r=a_q} \right] \\ &\quad \times a_q^2 \sin \theta \, d\theta \, d\phi \quad (14) \end{aligned}$$

which is in turn expressed by C_{qmn} and D_{qmn} . The absorption cross section is given by $\sigma^a = P^a/W^i = 2\zeta_0 P^a$.

The optical theorem states that the incident power in the forward direction is weakened due to the scattering and absorption, based on the law of energy conservation. The amount of this attenuation is called the extinction cross section and written as

$$\begin{aligned} \sigma^e &= \sigma^s + \sigma^a = -\frac{4\pi}{k_0^2} \operatorname{Im} [f_\theta(0, 0)] \approx \frac{2\pi}{k_0^2} \operatorname{Im} \left\{ \sum_{q=1}^Q e^{jk_0 z_{q0}} \right. \\ &\quad \left. \times \sum_{n=1}^{N_q} j^{n+1} n(n+1) [A_{q1n} + A_{q(-1)n} - B_{q1n} + B_{q(-1)n}] \right\} \quad (15) \end{aligned}$$

Suppose that Q spheres are present inside the volume V [m³]. Then we can compute the specific rain attenuation from $\gamma = \sigma^e/V$ [m⁻¹], with σ^e [m²] obtained from Eq. (15). Conversion into the practical unit is made by

$$\gamma \text{ [dB/km]} = \gamma \text{ [m}^{-1}\text{]} \times 10^3 \times 10 \log_{10} e = 4343 \sigma^e/V \quad (16)$$

2.4. Modeling of Raindrop Distribution

Let us determine the series of radii a_q as a function of rainfall intensity R [mm/h]. If $\mathcal{N}(a)$ [m⁻³ mm⁻¹] is the number of raindrops having the radius between a and $a + da$ [mm] per unit volume, then the integral

$$\tilde{\mathcal{N}}(a) = \int_0^a \mathcal{N}(a') da' \text{ [m}^{-3}\text{]} \quad (17)$$

gives the number of drops, the radii of which are less than a , per unit volume. When the number of drops taken into account in the numerical computation is Q , the radius a_q [mm] is sampled by the rule

$$\tilde{\mathcal{N}}(a_q)/\tilde{\mathcal{N}}(\infty) = (q - 1/2)/Q \quad (q = 1, 2, \dots, Q) \quad (18)$$

Among lots of proposed models, we select the Weibull distribution [17]

$$\mathcal{N}(a) = \mathcal{N}_0(\eta/\psi)(a/\psi)^{\eta-1} e^{-(a/\psi)^\eta} \quad (19)$$

where $\mathcal{N}_0 = 1000 \text{ m}^{-3} \text{ mm}^{-1}$, $\eta = 0.95 R^{0.14}$, and $\psi = 0.13 R^{0.44}$. Combination of Eqs. (18) and (19) yields

$$a_q = \psi \{-\log [1 - (q - 1/2)/Q]\}^{1/\eta} \text{ [mm]} \quad (20)$$

For example, if $R = 75$ mm/h and $Q = 8$, $a_q = 0.18, 0.35, 0.49, 0.63, 0.78, 0.95, 1.17, \text{ and } 1.56$ mm.

Suppose that Q drops are randomly distributed inside a fictitious sphere having the radius a^f [m] and the volume $V = 4\pi(a^f)^3/3 = Q/\tilde{\mathcal{N}}(\infty)$. For example, if $Q = 8$, the Weibull distribution gives $a^f = 0.124$ m regardless of R . Using uniform random numbers (ρ_1, ρ_2, ρ_3) falling in the interval $(0, 1)^3$, we allocate the center of the q -th sphere at $r_{q0} = a^f(\rho_1)^{1/3}$, $\theta_{q0} = \arccos(1 - 2\rho_2)$, and $\phi_{q0} = (2\rho_3 - 1)\pi$.

3. NUMERICAL RESULTS

3.1. Convergence of the Solution

3.1.1. Truncation Numbers

Table 1 shows the extinction cross sections computed from Eqs. (8) and (15) for three spheres with different radius a_q . The choice of

Table 1. Normalized extinction cross sections for three spheres aligned parallel to the x axis in the order of radius $(a_1, a_2, a_3) = (0.4, 0.8, 1.4)$ mm with 1 mm distance. The other parameters are $\varepsilon_r = 7.4 - j12.6$ and $f = 100$ GHz. “Dim.” is the dimension of Eq. (8), i.e., $4 \sum_{q=1}^3 N_q(N_q + 2)$.

Truncation	N_1	N_2	N_3	Dim.	$\sigma^e / \sum_{q=1}^3 (\pi a_q^2)$
Uniform	3	3	3	180	2.64418
	4	4	4	288	2.73732
	5	5	5	420	2.74814
	6	6	6	576	2.74902
	7	7	7	756	2.74908
Adaptive	4	5	7	488	2.74908

truncation numbers N_q is of two types: uniform and adaptive. In the latter case, we employed the criterion $N_q \approx 1 + k_0 a_q + 1.8(k_0 a_q)^{0.4}$. This was found by applying Debye’s asymptotic expansions into Mie’s coefficients for $|\varepsilon_r| \gg 1$ such that \bar{A}_{qn} and \bar{B}_{qn} in Eq. (9) keep four digits accuracy. The lowest two lines in Table 1 exhibit the same result, but the matrix size is reduced to $488/756 \approx 2/3$. The merit of this reduction becomes more remarkable when the number of spheres is increased.

The leftmost relation in Eq. (15) leads us to define the error on the optical theorem as

$$\epsilon^{\text{opt}} = 2 |\sigma^e - \sigma^s - \sigma^a| / |\sigma^e + \sigma^s + \sigma^a| \quad (21)$$

This value is, however, always zero or on the order of machine epsilon in the present numerical scheme, and thereby, we cannot use it as a tool of accuracy check. Nevertheless, Eq. (21) is a good indicator whether the double integral in Eq. (13) is precisely evaluated numerically. The integrals with respect to θ and ϕ are treated by the Gauss-Legendre quadrature rule and the trapezoidal formula, respectively. Numerical experiment told us that choosing the number of nodes as $\sum_{q=1}^3 N_q(N_q + 2)$ is enough for both arguments, unless spheres are very closely allocated.

3.1.2. Fineness of Drop Size Modeling

Let us discuss the relation between the specific rain attenuation and the number of sampled drops. In such examinations, it is enough to consider the case, for simplicity, where the drops are so sparsely distributed that the interaction effect is very weak. Therefore, in the

left hand side of Eq. (8), we neglect the triple sums which correspond to multiple scattering. This simplifies the solutions as

$$A_{qmn} \approx U_{mn} \bar{A}_{qn} e^{-jk_0 z_{q0}}, \quad B_{qmn} \approx V_{mn} \bar{B}_{qn} e^{-jk_0 z_{q0}} \quad (22)$$

Substituting the above expression into Eq. (15) and using Eq. (16), we have the approximate forms of extinction cross section and specific rain attenuation

$$\bar{\sigma}^e \approx -\frac{2\pi}{k_0^2} \operatorname{Re} \sum_{q=1}^Q \sum_{n=1}^{N_q} (2n+1) (\bar{A}_{qn} + \bar{B}_{qn}), \quad \bar{\gamma} = \frac{4343 \bar{\sigma}^e}{V} \text{ [dB/km]} \quad (23)$$

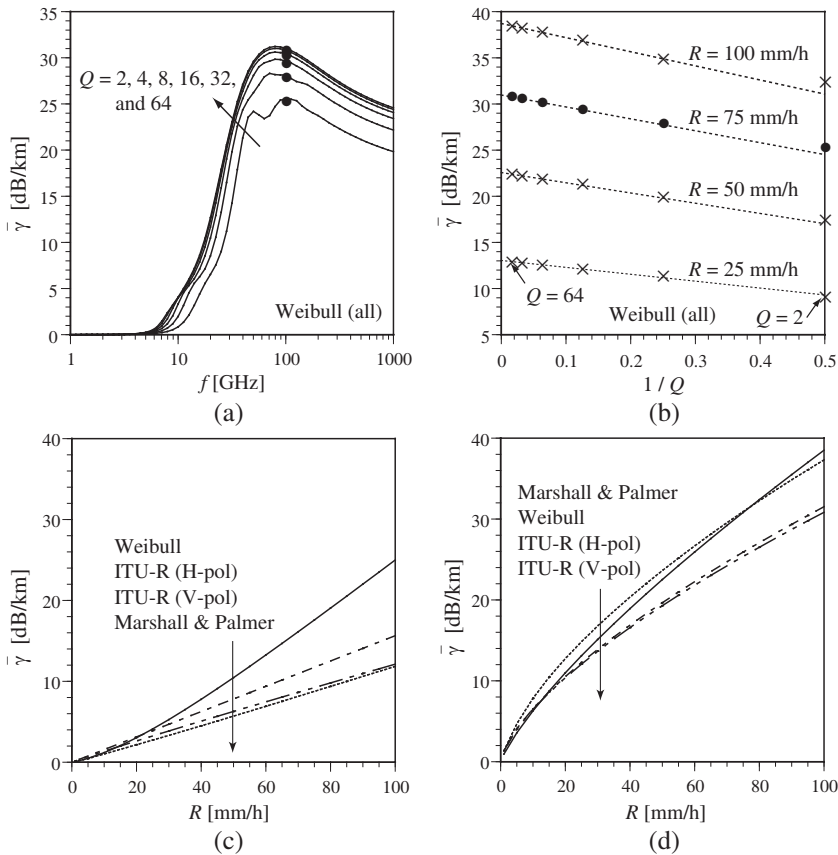


Figure 2. Dependence of specific rain attenuation $\bar{\gamma}$ on frequency f , rainfall intensity R , and number of sampled drops Q at 20°C . (a) $R = 75$ mm/h, (b) $f = 100$ GHz, (c) $f = 25$ GHz, and (d) $f = 100$ GHz. Circles denote common data for (a) and (b).

Figure 2 shows the behavior of rain attenuation for several parameters. The permittivity of water is a function of temperature and frequency, and one of the proposed formulas [19] gives, at 20°C, $\epsilon_r = 79.8 - j4.4$, $60.8 - j32.7$, $7.4 - j12.6$, and $4.0 - j2.2$ for 1, 10, 100, and 1000 GHz, respectively. Fig. 2(a) shows frequency dependence of $\bar{\gamma}$ for fixed R and several values of Q . The slight irregularity appears at $Q = 2$ by the internal resonance of dielectric media, but it is relaxed for larger Q due to field averaging. The distance between adjacent curves in Fig. 2(a) is nearly halved as Q is doubled, which brings about good convergence. This property is explicitly illustrated in Fig. 2(b) where the abscissa is $1/Q$. The plots for a fixed R are almost allocated in line. Though we can extrapolate $\bar{\gamma}$ as $Q \rightarrow \infty$ in Fig. 2(b), the curve at $Q = 32$ in Fig. 2(a) itself holds enough accuracy.

In Figs. 2(c) and (d), we compare our results with the ones based on the exponential model by Marshall and Palmer [15] and the ITU-R recommendation [21]. The curves except ITU-R do not include the polarization effect, since the simple spherical model was employed for them. We verified that these two distributions models predict close values of $\bar{\gamma}$ as f exceeds 80 GHz, and the same property was also reported in Fig. 1 of Ref. [18].

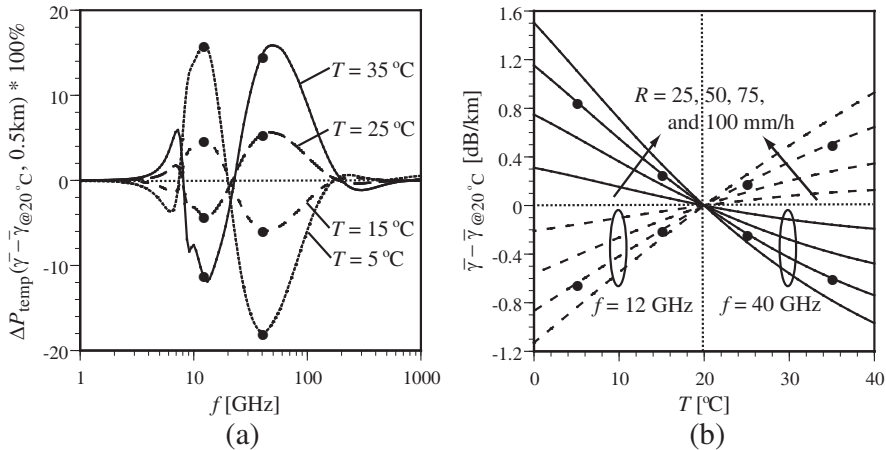


Figure 3. Deviation of specific rain attenuation $\bar{\gamma}$ from that value at 20°C based on the Weibull distribution. (a) Power difference in Eq. (24) at $R = 75$ mm/h, (b) $f = 12$ and 40 GHz. Circles denote the common data for (a) and (b).

Table 2. Complex conjugate of relative permittivity of water [19].

f [GHz]	$\epsilon_r^*_{@20^\circ\text{C}}$	$\epsilon_r^*_{@5^\circ\text{C}} - \epsilon_r^*_{@20^\circ\text{C}}$	$\epsilon_r^*_{@35^\circ\text{C}} - \epsilon_r^*_{@20^\circ\text{C}}$
12	$55.1 + j35.3$	$-14.1 + j4.5$	$+6.1 - j7.5$
22	$33.2 + j36.2$	$-12.3 - j4.7$	$+10.2 - j1.4$
40	$16.7 + j27.0$	$-5.7 - j6.8$	$+7.1 + j4.1$

3.2. Temperature Effect

Figure 3 shows the deviation of the rain attenuation γ from that at 20°C as a function of the frequency f , temperature T , and rainfall R . In order that the results may be deterministic, we neglect the multiple scattering effect which depends on the position of spheres. The number of sampled spheres, Q , is 32. Figure 3(a) displays the percentage difference of the attenuated powers

$$\Delta P_{\text{temp}}(\bar{\gamma} - \bar{\gamma}_{@T_0}, \ell) = \frac{e^{-2\bar{\gamma}\ell} - e^{-2\bar{\gamma}_{@T_0}\ell}}{e^{-2\bar{\gamma}_{@T_0}\ell}} \times 100\% \quad (24)$$

where ℓ [m] is the propagation length, $\bar{\gamma}$ [1/m] is the approximate attenuation constant, and T_0 is the temperature reference. If the units of $\bar{\gamma}$ and l are dB/m and m, respectively, $e^{-2\bar{\gamma}\ell}$ is replaced by $10^{-0.2\bar{\gamma}\ell}$. We choose a practical length $\ell = 0.5$ km, but the variation of ΔP_{temp} becomes large as ℓ increases. The curves tell us that the shift direction alternates at $f \approx 8, 22,$ and 180 GHz. Note that Fig. 7 of Ref. [4] shows this sort of behavior at $f \approx 8$ and 30 GHz at 25°C, but no data are given for $f > 40$ GHz. We can explain the property of Fig. 3(a) by observing the permittivity of water as in Table 2, where the complex conjugate is taken so that the positive large imaginary part may be related to increasing the absorption loss. The absorption seems, however, less effective than scattering. In fact, at 12 GHz, the raise of temperature increases the real part of ϵ_r ($-14.1 \rightarrow +6.1$ with 20°C base), leading to large scattering loss. On the other hand, at 40 GHz, the increase in the permittivity ($-5.7 \rightarrow +7.1$) makes the raindrops electrically large, which promotes the electromagnetic transparency of rain medium and results in low attenuation. The dependence on the rainfall intensity R is displayed in Fig. 3(b). As expected, the deviation is nearly proportional to R at a fixed temperature.

3.3. Effect of Multiple Scattering

From the viewpoint of ray optics, the major contribution of multiple scattering comes from doubly diffracted rays which hit two spheres.

Because the distribution of realistic raindrops is not so dense as that of snow, it is enough to take into account the double diffraction in order to discuss the deviation from the fields made by Mie's coefficients. In this situation, we can replace the expansion coefficients under the triple sum in Eq. (8) by their approximate expressions of Eq. (22). Then the solution is written in the closed form as

$$\begin{aligned} & \begin{pmatrix} A_{p\mu\nu}/\bar{A}_{p\nu} \\ B_{p\mu\nu}/\bar{B}_{p\nu} \end{pmatrix} = \begin{pmatrix} U_{\mu\nu} \\ V_{\mu\nu} \end{pmatrix} e^{-jk_0 z_{p0}} \\ & + \sum_{\substack{q=1 \\ (q \neq p)}}^Q \sum_{n=1}^{N_q} \sum_{m=\pm 1} \begin{pmatrix} U_{mn}\bar{A}_{qn} & V_{mn}\bar{B}_{qn} \\ V_{mn}\bar{B}_{qn} & U_{mn}\bar{A}_{qn} \end{pmatrix} \begin{pmatrix} \alpha_{mn,\mu\nu}^{(4)} \\ \beta_{mn,\mu\nu}^{(4)} \end{pmatrix} e^{-jk_0 z_{q0}} \quad (25) \end{aligned}$$

where the first and second terms in the right hand side correspond to singly and doubly diffracted rays, respectively. Note that m is limited to ± 1 in Eq. (25), since U_{mn} and V_{mn} vanish for the other m .

As before, we allocate Q raindrops in a fictitious sphere with radius a^f . This distribution model is, however, not enough, since there are an infinite number of drops around the fictitious sphere which can interact with the ones inside it. Therefore, we put additional $26Q$ spheres ($q = Q + 1, Q + 2, \dots, 27Q$) in the surrounding region $a^f < r < 3a^f$ with the same Weibull model, and take into account $27Q \times Q$ doubly diffracted rays. Here, the termination of the sum with respect to q in Eq. (25) is altered from Q to $27Q$. In order to reduce the CPU time, we ignore a part of rays which hit small drops and have negligible contribution to the results.

Figure 4 shows the percentage difference of the attenuated powers

$$\Delta P_{\text{mult}}(\gamma - \bar{\gamma}, \ell) = \frac{e^{-2\gamma\ell} - e^{-2\bar{\gamma}\ell}}{e^{-2\bar{\gamma}\ell}} \times 100\% \quad (26)$$

where ℓ [m] is the propagation length, and γ ($\bar{\gamma}$) [1/m] is the attenuation constant by the multiple (single) scattering model. The free space wavelength is roughly 1–100 mm. The number Q is fixed at 4, i.e., there are additional 104 drops in the surrounding region that cause multiple scattering. The computation is tried 32 times with randomly changing the position of spheres by the rule written in the last paragraph of Sec. 2.4. The size of them follows the Weibull distribution. The values of deviation at a fixed frequency are randomly distributed and almost equally divided into the plus and minus sides. This is because the phase shift determined by the distance between arbitrary two drops has random nature for each trial. Comparison of Figs. 4(a) and (b) tells us that the spread of deviation becomes large when the rainfall R increases.

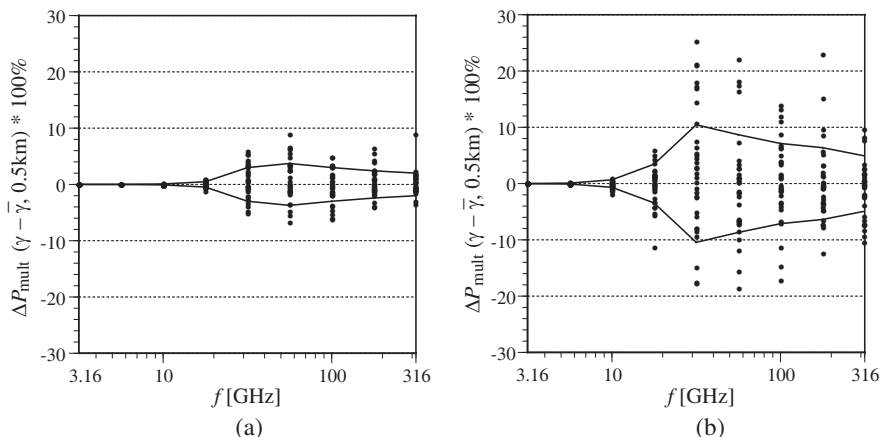


Figure 4. Traces of 32 trials for computing difference of attenuated power in Eq. (26), where multiple scattering is included (γ) and neglected ($\bar{\gamma}$) at 20°C. The symmetric pair of curves denote $\pm\Delta P_{\text{mult}}$ substituted by Eq. (27). (a) $R = 50$ mm/h, (b) $R = 100$ mm/h.

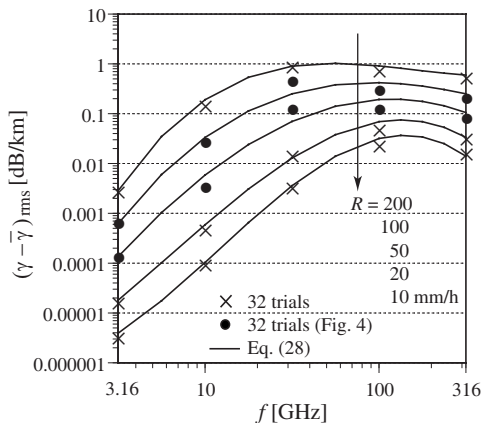


Figure 5. Root mean square of deviation of specific rain attenuation where multiple scattering is included (γ) and neglected ($\bar{\gamma}$).

The pair of curves running through the dots are drawn by the root mean square

$$(\gamma - \bar{\gamma})_{\text{rms}} = \sqrt{\frac{1}{I} \sum_{i=1}^I (\gamma_i - \bar{\gamma})^2} \tag{27}$$

where i is trial count and I is the number of trials, presently set at

32. About 70% of the dots are held between the \pm rms curves, which nearly obeys the normal distribution. Note that rms value has a peak at about 60 and 30 GHz for 50 and 100 mm/h, respectively.

Figure 5 shows the rms of rain attenuation for a wide range of rainfall: The data for $R = 10, 20,$ and 200 mm/h are supplemented to Fig. 4. The results by numerical experiment of 32 trials are plotted by crosses and circles, the latter of which are quoted from Fig. 4. We constructed the function fitting the above marks as

$$(\gamma - \bar{\gamma})_{\text{rms}} = 10^{(-0.58 + 1.22\tilde{R})\tilde{f}^3 + (1.39 - 5.61\tilde{R})\tilde{f}^2 + (1.96 + 6.90\tilde{R})\tilde{f} - 6.00} \text{ [dB/km]} \quad (28)$$

where

$$\tilde{f} = \log_{10} f, \quad \tilde{R} = \log_{10}(R/20) \quad (29)$$

with f and R measured in GHz and mm/h, respectively. The rms values first increase in the range 1–30 GHz, then saturate or even decrease a little in the rest. The peak shifts to the low frequency side when the rainfall becomes strong. The maximum rms mounts to 1 dB/km at 200 mm/h and 31.6 GHz, corresponding to the power fluctuation of signal by $10^{-0.2} \approx 63\%$.

4. CONCLUSION

The multipole expansion solution has been developed to the problem of scattering and absorption for arbitrarily allocated dielectric spheres with different size. We derived the set of linear equations for the expansion coefficients and demonstrated the effectiveness of choosing truncation numbers in an adaptive manner. Computed extinction cross sections lead directly to the specific rain attenuation, where the Weibull raindrop distribution formula is used. After the check on numerical convergence, we computed the value of rain attenuation by changing temperature and by taking multiple scattering into account. It is found that the dependence of the permittivity of water on temperature and frequency affects the attenuation property. We also note that the effect of multiple scattering becomes highest between microwave and millimeter wave bands, i.e., 30–200 GHz, which is contrary to previously accepted belief that the multiple scattering become evident above several hundred gigahertz.

The present results and discussions will become more convincing if we deal with raindrops of realistic shape [4]. Numerical analysis of a set of such deformed bodies may be done by the transition matrix method [22]. The Yasuura method would be effective as well, including out-going and in-coming wave functions, which is a spherical coordinate version of the deep grating case [23] where up- and down-going waves are considered. This problem deserves further attention.

ACKNOWLEDGMENT

The authors gratefully acknowledge financial support for long term training program from Japan International Cooperation Agency (JICA).

REFERENCES

1. Brussaard, G. and P. A. Watson, *Atmospheric Modelling and Millimetre Wave Propagation*, Sec. 4.2, Chapman & Hall, London, 1994.
2. Lin, D.-P. and H.-Y. Chen, "An empirical formula for the prediction of rain attenuation in frequency range 0.6–100 GHz," *IEEE Trans. Antennas Propagat.*, Vol. 50, No. 4, 545–551, 2002.
3. Zhu, L., X.-G. Li, and G.-W. Lou, "Analysis of characters of submillimeter wave attenuation by rain medium," *Microwave Opt. Tech. Lett.*, Vol. 50, No. 4, 1025–1028, 2008.
4. Bahrami, M. and J. Rashed-Mohassel, "An exact solution of coherent wave propagation in rain medium with realistic raindrop shapes," *Progress In Electromagnetics Research*, PIER 79, 107–118, 2008.
5. Oguchi, T., "Scattering properties of Pruppacher-and-Pitter form raindrops and cross polarization due to rain: Calculation at 11, 13, 19.3, and 34.8 GHz," *Radio Science*, Vol. 12, No. 1, 41–51, 1977.
6. Ishimaru, A., "Multiple scattering calculations of rain effects," *Radio Science*, Vol. 17, No. 6, 1425–1433, 1982.
7. Tsolakis, A. I. and W. L. Stutzman, "Multiple scattering of electromagnetic waves by rain," *Radio Science*, Vol. 17, No. 6, 1495–1502, 1982.
8. Rogers, D. V. and R. L. Olsen, "Multiple scattering in coherent radiowave propagation through rain," *COMSAT Technical Review*, Vol. 13, 385–401, 1983.
9. Pruppacher, H. R. and R. L. Pitter, "A semi-empirical determination of the shape of cloud and rain drops," *J. Atmos. Sci.*, Vol. 28, No. 1, 86–94, 1971.
10. Bruning, J. H. and Y. T. Lo, "Multiple scattering of EM waves by spheres part I — Multipole expansion and ray-optical solutions," *IEEE Trans. Antennas Propag.*, Vol. 19, No. 3, 378–390, 1971.
11. Hamid, A.-K., I. R. Ciric, and M. Hamid, "Electromagnetic scattering by an arbitrary configuration of dielectric spheres," *Can. J. Phys.*, Vol. 68, No. 12, 1419–1428, 1990.

12. Matsushima, A., Y. Momoka, M. Ohtsu, and Y. Okuno, "Efficient numerical approach to electromagnetic scattering from three-dimensional periodic array of dielectric spheres using sequential accumulation," *Progress In Electromagnetics Research*, PIER 69, 305–322, 2007.
13. Stratton, J. A., *Electromagnetic Theory*, Ch. 7, McGraw-Hill, NY, 1941.
14. Cruzan, O. R., "Translation addition theorem for spherical vector wave functions," *Quart. J. Appl. Math.*, Vol. 20, 33–39, 1962.
15. Marshall, J. S. and W. M. Palmer, "The distribution of raindrops with size," *J. Meteorology*, Vol. 5, 165–166, 1948.
16. Atlas, D. and C. W. Ulbrich, "The physical basis for attenuation rainfall relationships and the measurement of rainfall parameters by combined attenuation and radar methods," *J. Rech. Atmos.*, Vol. 8, 275–298, 1974.
17. Sekine, M., C.-D. Chen, and T. Musha, "Rain attenuation from log-normal and weibull raindrop-size distributions," *IEEE Trans. Antennas Propagat.*, Vol. 35, No. 3, 358–359, 1987.
18. Utsunomiya, T. and M. Sekine, "Rain attenuation at millimeter and submillimeter wavelengths," *Int. J. Infrared Millimeter Waves*, Vol. 26, No. 6, 905–920, 2005.
19. Liebe, H. J., G. A. Hufford, and T. Manabe, "A Model for the complex permittivity of water at frequencies below 1 THz," *Int. J. Infrared Millimeter Waves*, Vol. 12, No. 7, 659–675, 1991.
20. Harrington, R. F., *Time-harmonic Electromagnetic Fields*, Ch. 3, McGraw-Hill, NY, 1961.
21. ITU-R P.838-3, "Specific attenuation model for rain for use in prediction methods," May 2005.
22. Waterman, P. C., "Matrix formulation of electromagnetic scattering," *Proc. IEEE*, Vol. 53, 805–812, 1965.
23. Ohtsu, M., Y. Okuno, A. Matsushima, and T. Suyama, "A combination of up- and down-going Floquet modal functions used to describe the field inside grooves of a deep grating," *Progress In Electromagnetics Research*, PIER 64, 293–316, 2006.